Reconfigurable origami sonic barriers with tunable bandgaps for traffic noise mitigation

M. Thota, and K. W. Wang

Citation: Journal of Applied Physics **122**, 154901 (2017);
View online: https://doi.org/10.1063/1.4991026
View Table of Contents: http://aip.scitation.org/toc/jap/122/15
Published by the American Institute of Physics

JOURNAL OF APPLIED PHYSICS **122**, 154901 (2017)

Reconfigurable origami sonic barriers with tunable bandgaps for traffic noise mitigation

M. Thota[a] and K. W. Wang
Department of Mechanical Engineering, University of Michigan, Ann Arbor, Michigan 48109, USA

(Received 19 June 2017; accepted 14 September 2017; published online 17 October 2017)

An origami sonic barrier composed of cylindrical inclusions attached onto an origami sheet is proposed. The idea allows for tunable sound blocking properties for application in attenuating complex traffic noise spectra. Folding of the underlying origami sheet transforms the periodicity of the inclusions between different Bravais lattices, viz. between a square and a hexagonal lattice, and such significant lattice re-configuration leads to drastic tuning of dispersion characteristics. The wave tuning capabilities are corroborated via performing theoretical and numerical investigations using a plane wave expansion method and an acoustic simulation package of COMSOL, while experiments are performed on a one-seventh scaled-down model of origami sonic barrier to demonstrate the lattice re-configuration between different Bravais lattices and the associated bandgap adaptability. Good sound blocking performance in the frequency range of traffic noise spectra combined with less efforts, required for actuating one-degree of freedom folding mechanism, makes the origami sonic barrier a potential candidate for mitigating complex traffic noise. *Published by AIP Publishing*. https://doi.org/10.1063/1.4991026

I. INTRODUCTION

With the increase in urban population, the number of vehicles on the road has increased exponentially, and the associated traffic noise pollution is also peaking. Noise pollution is defined as harmful level of sound that disturbs the natural rhythm of the human body, and traffic noise is considered one of the major sources of noise pollution in an urban environment. Several studies have shown that high intensity noise is the cause of many health issues such as sleep apnea, stress, fatigue and hypertension.[1,2] Apart from health issues, traffic noise also interferes with cognitive functions including attention, concentration, memory, reading ability, and sound discrimination—leading to a less productive work environment.

The main source of traffic noise, which is the vehicle pass-by noise, comes from sources such as engine, intake and exhaust manifolds, tire-road interaction, road surface quality and other engine accessories.[3] It is further known that the frequencies of the noise sources depend on the following two factors (a) *type of vehicle*: heavy-duty vehicles such as freight trucks, buses and lorries produce low frequency noise, while light vehicles such as automobiles and motor cycles create high frequency sound and (b) *speed of vehicle*: vehicles travelling at low speed (for example, on highways during rush hour traffic) contributes to low frequency traffic noise, while on the other hand, vehicles travelling at high speed (for example, on highways during off-peak traffic) lead to traffic noise dominated by high frequency content. It has been quantified that these variations under traffic conditions cause the dominant frequency of the noise spectra to shift between 500 and 1200 (Hz).[4–6] Hence, an effective sonic barrier needs to be able to adapt and attenuate the dynamically changing dominant traffic noise spectra to reduce the harmful effects of noise pollution.

While the traditional barriers such as vertical walls that act as barriers can attenuate the traffic noise across the entire spectrum, they are heavy and block the flow of wind which may lead to high loads and moments on the foundation upon which it is built, thereby limiting its applications. Secondly, the design of vertical walls to block the sound across a broad range of frequencies is an overkill strategy, as the traffic conditions that create noise across the entire spectrum seldom occur. Finally, the incidence of oblique waves onto these barriers leads to higher diffraction at the top edge and increases the noise propagation across the barrier, compared to barriers (developed in this work) that have a rough top edge.[7–9] The second kind of sound barriers is made of periodic structures,[10–24] and some on-road installations [Fig. 1(a)][29] have shown that the periodic barriers can be used to block the sound wave propagation. Some of the benefits of periodic sonic barriers include (a) a less amount of load transfer to foundation on which it is built, (b) being optically transparent and permeable to wind and (c) having an aesthetically pleasing view.[10,11] However, one of the major drawbacks of these designs is that, with fixed periodicity, the barriers can only block traffic noise spectra corresponding to certain frequency range that is dictated by Bragg's effect. In order to elevate this problem, recent studies proposed periodic barriers that possess multi-physical phenomena properties that improve the attenuation range[11,15,17,19,23] [Fig. 1(a)]. But the attenuation phenomena, such as absorption and resonance, in the modern barriers require the use of a sophisticated barrier material, and the construction process is complicated.

Building upon the benefits of periodic barriers and to elevate the inherent problem of fixed periodicity in their

[a]Author to whom the correspondence should be addressed: mthota@umich.edu. Tel.: 734-680-4265.

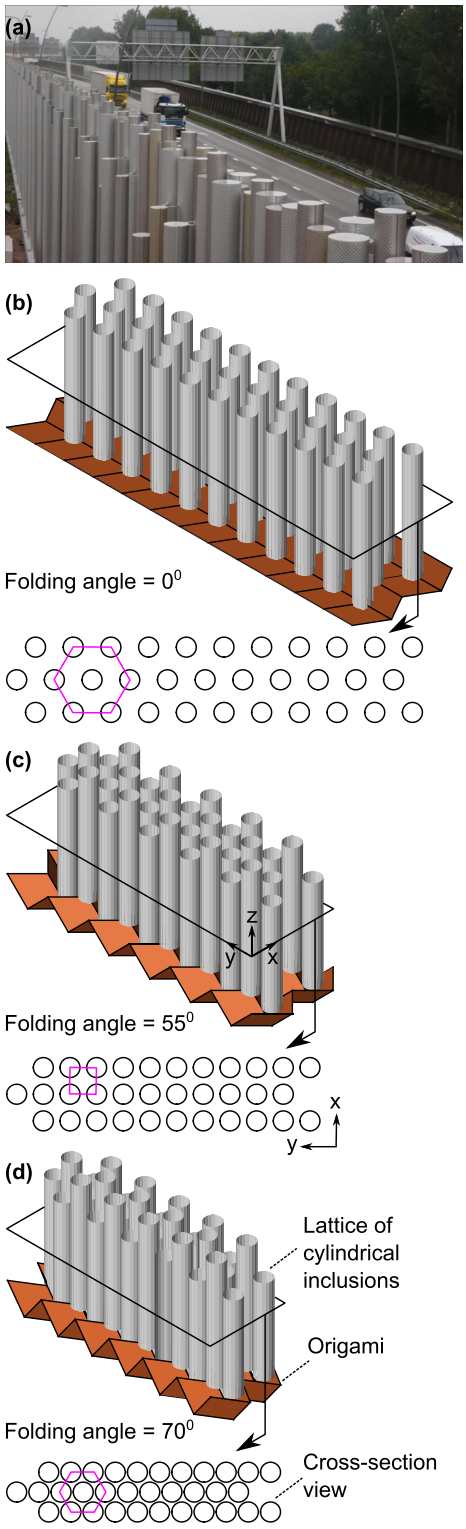

FIG. 1. (a) Periodic pipe noise barrier installed in Eindhoven by Van Campen.[29] (b) and (c) Illustrations of different folding configurations of an origami sonic barrier (OSB) and their corresponding cross-section views. The pink polygons in cross-section views identify different lattice patterns and show that the lattice transforms from a (b) hexagon to a (c) square and to a (d) hexagon, when the folding angle is shifted from (b) 0° to (c) 55° and to (d) 70°.

design, here, we propose an innovative design of a reconfigurable periodic barrier and utilize the effect of varying periodicity to efficiently block the dynamically changing traffic noise spectra. In our previous theoretical work,[25] we have shown that the periodicity of a lattice of inclusions can be varied by folding the underlying origami architecture. Based on this concept, here, we propose a new design of reconfigurable origami sonic barrier (OSB) that constitutes periodically arranged cylindrical inclusions attached on top of an origami sheet. In this work, the origami folding kinematics are designed such that the reconfiguration in the periodicity of inclusions occurs between distinct symmetry properties (such as square and hexagonal Bravais lattice patterns). Such folding induced reconfigurations are shown to drastically change the spectral properties of bandgaps, and are exploited to block the dynamically changing traffic noise spectra. Furthermore, the origami folding, being a simple one-degree of freedom action, requires only minimal local actuation to effectively change the global shape. In this study, a scaled-down OSB is built, and its tunable sound blocking performance is demonstrated. Overall, the versatile and practical-to-implement origami design is exploited to build an ideal reconfigurable sonic barrier for managing a complex traffic noise pattern.

In this article, we first describe the design of an origami sonic barrier (Sec. II) followed by analytical and numerical simulation results demonstrating tunable bandgap features (Sec. III). We then explain the details of the design and fabrication of an origami sonic barrier and present test results that show adaptability in sound blocking features (Sec. IV). We then discuss the correlation between results and conclude the article with some final remarks (Sec. V).

II. CONCEPT

To achieve lattice transformation, the origami sonic barrier (OSB) is made up of rigid cylindrical inclusions attached onto the vertices of a Miura-origami sheet [Figs. 1(b)–1(d)]. As shown in the illustrations, the folding induced kinematics leads to transformation in the periodicity of inclusions between different lattice patterns [refer to the cross-section views of Figs. 1(b)–1(d)].

The periodic Miura-origami sheet can be studied via a unit vertex (Fig. 2), where the following three parameters completely define the geometry of an origami sheet; two crease lengths (a,b) and one sector angle (γ) between them. To study the folding kinematics of the origami sheet, a dihedral folding angle (θ) that represents the angle made by quadrilateral facets with the xy reference plane is considered. When the folding angle is 0°, the origami sheet is completely flat and parallel to the xy plane, while on the other hand, when the folding angle is 90°, the origami sheet again collapses into a flat sheet that is perpendicular to the xy plane. As a result, the relative spatial position of the origami vertices

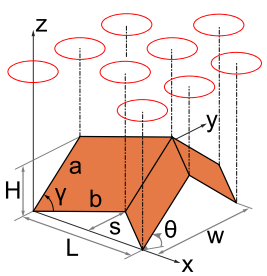

FIG. 2. Origami unit vertex labelled with important geometric parameters.

changes with the folding angle, and their kinematic relations are given by Eq. (1). Since the inclusions are attached on top of origami vertices (represented by red ellipses in Fig. 2), the periodic geometric distribution of inclusions also changes with the folding angle.

$$\begin{aligned} H &= a\sin\theta\sin\gamma, \\ L &= \frac{2b\cos\theta\sin\gamma}{\sqrt{1-\sin^2\theta\sin^2\gamma}}, \\ W &= 2a\sqrt{1-\sin^2\theta\sin^2\gamma}, \\ S &= \frac{b\cos\gamma}{\sqrt{1-\sin^2\theta\sin^2\gamma}}. \end{aligned} \tag{1}$$

To achieve large adaptation in the sound blocking performance required for mitigating dynamically changing traffic noise spectra that vary between 500 and 1200 (Hz), we design the origami sheet such that the folding kinematics can change the periodicity of inclusions between square and hexagonal lattice patterns. As will be shown later, such transformations between lattice patterns with distinct symmetry properties can lead to a drastic adaptation in the spectral properties of bandgaps. In this regard, to achieve desired lattice patterns in the spatial distribution of inclusions attached onto the vertices of the Miura-origami sheet, the following relations [Eq. (2)] between origami geometric parameters must be met.

To achieve a square lattice pattern

$$\frac{a}{b} = \frac{n}{\cos\gamma\,(n^2+1)}, \tag{2}$$

where n is an integer.

To achieve a hexagonal lattice pattern

$$\frac{a}{b} = \frac{2(2n-1)}{\cos\gamma\left((2n-1)^2+3\right)}.$$

Solving the above equations for $n=1$ to 6, we generate Fig. 3 that provides a parametric design space of the origami sheet; these design parameters can achieve either a square, hexagonal or both patterns in the lattice of inclusions attached onto the vertices of Miura-origami sheet. In Fig. 3, the black dashed curves provide the origami sheet design parameters that can achieve a hexagonal lattice pattern, while the red dash-dotted curves represent design parameters that can achieve a square lattice pattern. It can also be seen from Fig. 3 that for some design parameters (marked by a thick green dash-dotted curve), it is possible to achieve both square and hexagonal configurations; i.e., by folding the Miura-origami designs on a thick green dash-dotted line, the lattice of inclusions can transform between square and hexagonal patterns.

Among the possible designs available (thick green-dash dotted line), as a proof of concept, we pick an origami sheet design represented by a circular marker that can transform between square and hexagonal lattice patterns; the circular marker represents the design with a crease length ratio (a/b) of 1 and a sector angle (γ) of 60°. As will be shown later,

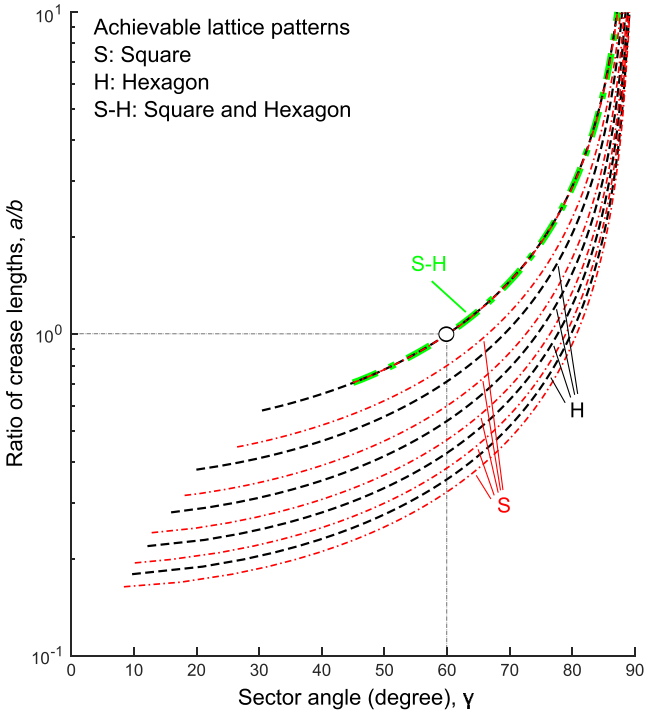

FIG. 3. Achievable lattice configurations via Miura-Origami rigid folding based on different crease designs. Combinations of γ and a/b that can achieve a hexagonal lattice (H) and a square lattice (S) are represented by black dashed and red dashed-dotted curves respectively. Only the curves based on n = 1 to 6 are plotted. There exists a subset of γ and a/b combinations (thick green dash-dotted curve), where it is possible to switch between square (S) and hexagonal (H) lattice types.

this design with the following values for the crease lengths $a(=b)$ and the radius (R) of cylindrical inclusions, 0.56 (m) and 0.1477 (m) respectively, will block the dominant traffic noise spectra i.e., varying between 500 and 1200 (Hz). To demonstrate the lattice transformation, we illustrate the spatial distribution of inclusions in an OSB with the circular marker design in Figs. 1(b)–1(d); for the chosen set of parameters, the lattice of the inclusions is transformed from a hexagon into a square, and then to a hexagon pattern, when the folding angle is varied from 0° to 55° to 70° respectively. In this work, the cylindrical inclusions are made of polyvinyl chloride (PVC) material, and the OSB is placed in air that acts as the host media in which sound propagation is evaluated.

III. ANALYTICAL AND NUMERICAL INVESTIGATIONS

A. Analytical investigation via a plane wave expansion (PWE) method

In order to study the effect of lattice reconfiguration on the bandgap features of an OSB, the first principle wave equation [Eq. (3)] is solved via the PWE method. The OSB is assumed to be large in the axis parallel to the inclusions and we only solve for the acoustic wave propagation through the plane perpendicular to the inclusion axis. The OSB being periodic in the xy plane, its wave behavior can be evaluated by solving the wave equations [Eq. (3)] inside a unit-cell with appropriate boundary conditions [Fig. 4(a)]. This unit-cell, as represented by a dashed rectangle in Fig. 4(a),

consists of a basis that is formed by two inclusions marked with centers at C_1 and C_2, and is composed of two lattice vectors a_1 and a_2; tessellations of this unit-cell combined with basis inclusions along a_1 and a_2 directions will re-create the origami sonic barrier. The relationship between the unit-cell parameters and the origami unit vertex parameters is given in Eq. (4),

$$\left(\frac{1}{\rho c_l^2}\right)\frac{\partial^2 p}{\partial t^2} = \nabla.\left(\frac{1}{\rho}\nabla p\right), \tag{3}$$

$$\begin{aligned} \vec{a_1} &= L\hat{x}, \\ \vec{a_2} &= \frac{W}{2}\hat{y}, \\ \vec{C_1} &= \frac{|a_1|}{2}\hat{a_1} + \frac{|a_2|}{2}\hat{a_2}, \\ \vec{C_2} &= \left(s - \frac{3|a_2|}{2}\right)\hat{a_2}. \end{aligned} \tag{4}$$

The materials properties of PVC inclusions and the air host are given in Table I. Because of the high impedance mismatch between the solid inclusions and the fluid host, most of the wave energy incident onto the inclusions will be reflected. With little energy transfer into the inclusions, we can ignore any transverse vibrations and model the solid material as an equivalent media that can only sustain longitudinal wave propagation. Furthermore, the host is assumed to be ideal and does not dissipate any wave energy passing through it.

The general idea behind the PWE method[26,27] is to expand the materials properties ($\rho_{inv} = \frac{1}{\rho}$, $K_{inv} = \frac{1}{\rho c_l^2}$) and the pressure wavefield (p) in Eq. (3), in terms of Fourier series expansion. Upon substitution of series expansion into the first principle partial differential equation (PDE) [Eq. (3)], it can be converted into an eigenvalue problem (EVP) with two variables; viz. wavevector ($\boldsymbol{k}$) and eigen frequency. The wavevector is swept along the high-symmetry directions of reduced 1st Brillouin zone [given in the inset of Fig. 4(a)], and the eigen frequencies are evaluated to extract the dispersion diagrams as shown in Figs. 5(b) and 5(d); more details about the PWE method can be found in Appendix A.

Dispersion diagrams of an OSB in two different configurations given in Figs. 1(c) and 1(d) are plotted in Figs. 5(b) and 5(d) respectively. Discontinuities in dispersion diagrams across all high symmetry edges of the reduced 1st Brillouin zone represent complete bandgaps,[28] and are highlighted as a region between horizontal dash-dotted (blue) lines in Figs. 5(b) and 5(d); in such spectral regions, sound propagation is blocked for all wave incidence directions. From these plots, it can be clearly seen that the bandgap of an OSB at 55° and 70° folding configurations occur around 500 and 1000 (Hz) respectively. The significant shift in the bandgap during folding, especially in the 500–1200 (Hz) range, could be very useful for attenuating the dynamically changing traffic noise spectra.

TABLE I. Materials properties of inclusions and the host.

Materials properties	PVC	Air
Density, (ρ), (kg/m^3)	1.56×10^3	1.3
Longitudinal speed of sound (c_l) (m/s)	2395	340

B. Numerical investigation via finite element analysis (FEA)

The dispersion diagrams extracted via the PWE method are for infinitely periodic structures, but in real situations, finite sample effects have to be taken into account. For this reason, numerical simulations are performed on a finite sample using commercial FEA software COMSOL.

For this study, the 2D cross-section of an OSB in two different configurations, as given in Figs. 4(b) and 4(c), is modelled and evaluated using the acoustic-structural interface package of COMSOL. As before, the circular solid inclusions and the fluid host are provided with materials properties corresponding to PVC and air, as given in Table I. In this model, the locations of a point source and receivers are also shown, where the source is placed at a distance of 2 (m) from the first row of OSB, and the sound pressure level (SPL) is measured at receivers, which are placed at a distance of 4 (m) from the source. The two receivers are positioned such that, each of the source-receiver line makes an angle of 0° and 45° with respect to the x-axis; measurements from these two different receivers are required to calculate the insertion loss (IL) of transmission along different wave directions. In this model, the four outside boundaries of the model are provided with the radiation boundary condition to absorb any reflections.

A frequency domain analysis is performed across the frequency range 10–1500 (Hz), and the insertion loss (IL), which is extracted as the difference in SPL (in dB) without and with a sonic barrier, is plotted in Figs. 5(a) and 5(c). Each figure contains two IL curves, solid (purple) and dash-dotted (green), representing 0° and 45° wave excitations, respectively, and a higher value of IL in each of these curves

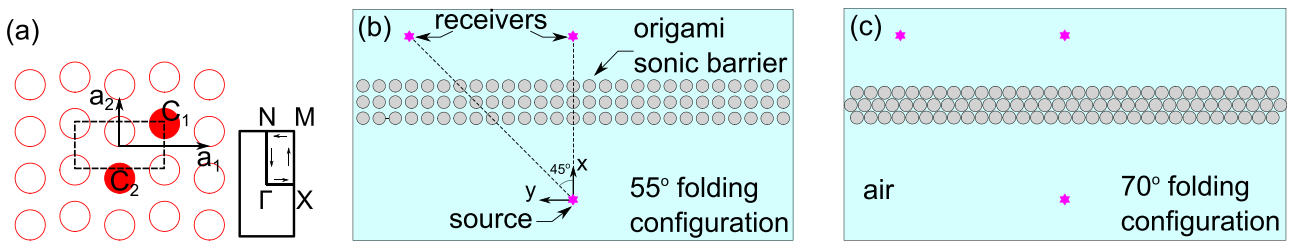

FIG. 4. (a) Description of a unit cell and a reduced 1st Brillouin zone used for the PWE method. (b) and (c) Models developed in COMSOL for evaluating the insertion loss (IL) spectra of an origami sonic barrier (OSB) at two different folding configurations.

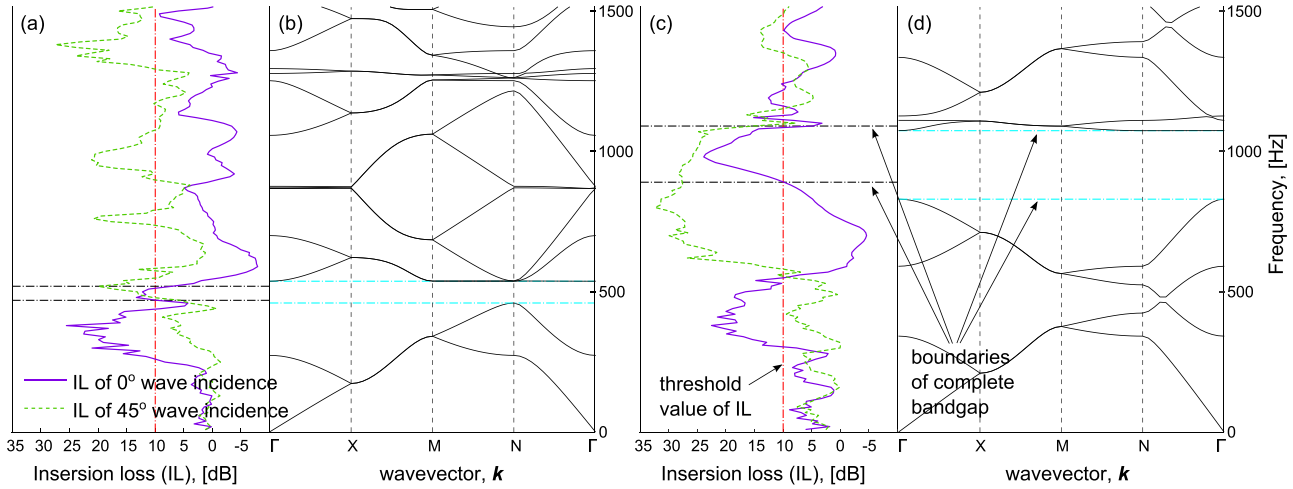

FIG. 5. (a) and (c) are the insertion loss (IL) spectra evaluated via numerical simulations in COMSOL, and (b) and (d) are the dispersion diagrams generated via the PWE method of an origami sonic barrier (OSB) at 55° and 70° folding angles, respectively. In (a) and (c), two different IL curves correspond to 0° and 45° wave incidence.

represents good sound blocking performance; in general, a sound barrier with an IL of 10 (dB) is considered of good quality,[18] and a vertical dash-dotted (red) line is plotted in Figs. 5(a) and 5(c) as a guide, indicating the threshold IL. For qualitative reference, a 10 (dB) drop in IL would be equivalent to cutting noise pressure levels by 90%, or to put it in other words, the traffic noise that could otherwise be heard as far as a mile away would now only be perceived from a distance of 0.3 miles. It can be clearly seen that the sound blocking phenomena of an OSB at 55° and 70° configurations occur in different spectral regions with the IL peaking at 500 and 1000 (Hz), respectively; these regions are marked by horizontal dash-dotted (black) lines in Figs. 5(a)–5(c), where the IL is greater than the threshold for both wave incidence directions. These spectral regions with a high IL match very well with the complete bandgaps predicted via the PWE method, and provide further evidence of adaptability in the sound blocking performance of an OSB.

Overall, the above analytical and numerical investigation results show that for traffic noise dominated by low frequency content [around 500 (Hz)], the OSB can be configured to 55° folding angle, while on the other hand, the OSB in 70° configuration can be used to block traffic noise dominated by high frequency content [around 1000 (Hz)]—making the origami sonic barrier effective in blocking the dynamically changing traffic noise spectra. It should be noted that the above analytical and numerical results, in terms of dispersion plots and IL spectra, are independent of the density ratio between the solid inclusions and the fluid host if the density ratios are higher than 100 (Ref. 26) (the density ratio of the system used in this paper is around 1200).

IV. EXPERIMENTAL INVESTIGATION

A. Scaled-down model

To experimentally demonstrate the lattice reconfiguration and adaptable sound blocking features, we have fabricated and performed tests on a scaled-down model of OSB in an anechoic chamber (Fig. 6). More precisely, a one-seventh model is constructed with the following origami unit vertex parameters; crease lengths ($a = b$) of 0.08 (m) and a sector angle (γ) of 60°. Being a linear system, the result of this proof-of-concept scaled-down model should be enough to demonstrate the concept and understand the behavior of a full scale sonic barrier.

B. Fabrication details

The following raw materials and process are used during fabrication: facets of the origami sheet are made by water-jet cutting of the aluminum sheet of 0.05 (in) thickness, and the individual facets are arranged together to form an origami sheet using an ultra-high molecular weight (UHMW) polythene adhesive sheet of 0.005 (in) thickness; during the folding process, the UHMW polythene folds at the crease lines, while the facets remain rigid. 1 1/4 (in) PVC pipes with an outer radius of 0.0211 (m) are used as cylindrical inclusions, and 360° friction hinges are attached to the origami vertices that hold the PVC pipes up-right and move them as per the trajectory of origami vertices during the folding process. Finally, a caster pipe cap assembly is used as a connector between PVC pipes and friction hinges.

The OSB that is folded into different configurations is shown in Fig. 6, where different views of the barrier are given. In the iso-view [Figs. 6(a)–6(c)], different parts of the construction are labelled, and a close-up view of the origami sheet at 0°, 55° and 70° folding configurations is given; it should be noted that the origami sheet is flat on the table at 0° folding angle [Fig. 6(a)], and as the folding angle increases, the quadrilateral facets gradually raise making an angle with the table [Figs. 6(b) and 6(c)]. Through the top views [Figs. 6(d)–6(f)], it can be clearly seen that the periodic spatial distribution of the inclusions in the xy plane transforms from a hexagon, to a square and finally to a hexagon Bravais lattice when the folding angle changes from 0° to 55° to 70°, as predicted through kinematic relations given in Eq. (1); in these figures, green polygons are drawn as a guide to identify the lattice shapes. In this top view, we can

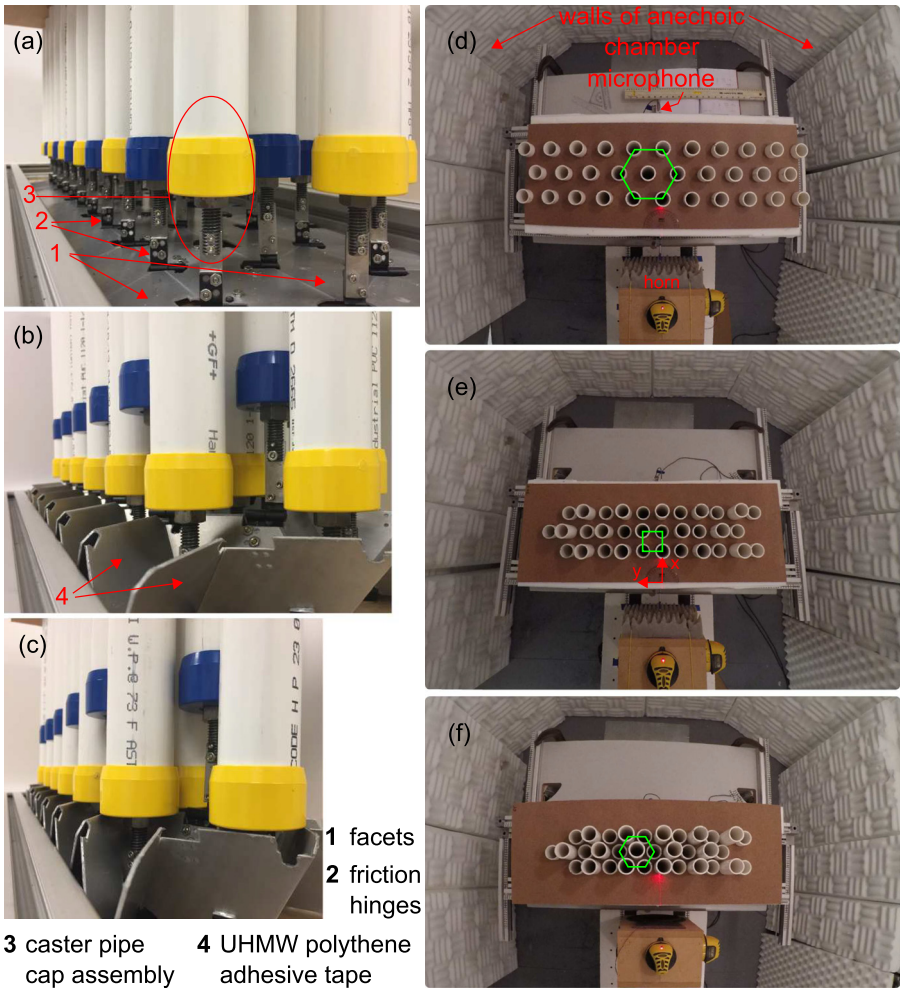

FIG. 6. Different folding configurations of a scaled-down origami sonic barrier (OSB). (a)–(c) and (d)–(f) are isometric and top views of the origami sonic barrier (OSB) at 0°, 55° and 70° folding angles respectively.

also see the walls of the anechoic chamber, in which the experiment is conducted.

In order to measure the insertion loss (IL) due to the transmission of a 2D propagating wave, sufficient foam is added at the top and the bottom of the pipes [as shown in the side view, Fig. 7(a)], so that the oblique waves incident onto the sonic barrier from the source are absorbed. Furthermore, to minimize the dispersion of the incident wave in the z-direction, a horn (Piezo source #KSN1141A) with a rectangular aspect ratio is chosen as a source that would focus the sound energy predominantly in the xy plane. Finally, to record the pressure of waves after passing through the sonic barrier, a microphone [Larson-Davis $^1/_4$ (in) microphone #2520] is placed behind the sonic barrier [shown in Fig. 7(a)]. While the horn and the microphone are placed at the same level in the z-direction equi-distant from top and bottom foams, they are placed at a distance of 18 (cm) in front, and 2 (cm) behind the sonic barrier along the x-direction, respectively, as given in the schematic in Fig. 7(b).

C. Test method

Random white noise is generated through the horn, and the pressure is recorded using the microphone, where NI DAQ and LabVIEW are used for both generation and acquisition of analog signals at a sampling rate of 1 (MHz). The 0.1 (s) time series signal from the microphone is extracted for calculating FFT spectra, and the spectra is averaged over 20 (s) of data to improve the signal to noise ratio. For each OSB configuration, the test is repeated two times with a horn-mic configuration (a) parallel to the x-axis and passing through the center of the sample (viz. 0° excitation) and (b) at an angle of 45°, with respect to the x-axis (viz. 45° excitation), as shown in the schematic of Fig. 7(b) and during the test in Figs. 7(c) and 7(d); these different experiments are required to test the barrier performance to incident waves traveling in different directions. The experimental results of 0° and 45° wave excitations of OSB at 55° and 70° folding angle configurations are shown in Fig. 8(a) and 8(c), where the IL (in dB) curves are calculated as the ratio of pressure spectra without and with the sonic barrier. Since the horn has a smooth response in the 2–30 (kHz) range, the IL of transmission is shown from 2.5 (kHz) and is cut-off at 10.5 (kHz). Moreover, since the frequency can be normalized as $\omega x/c_l$ (where "c_l" is the speed of sound in air and "x" represents the lattice constant parameter) while solving the wave equations,[25] this spectral range of 2.5–10.5 (kHz) in these validation tests of 1:7 scaled-down model also corresponds to the frequency range of 350–1500 (Hz) in the actual size sonic barrier, which is where the traffic noise spectra are known to vary.

D. Results and discussion

In Figs. 8(a) and 8(c), the solid (purple) and dash-dotted (green) curves represent the spectra corresponding to 0° and 45° excitations, respectively, and the vertical dash-dotted

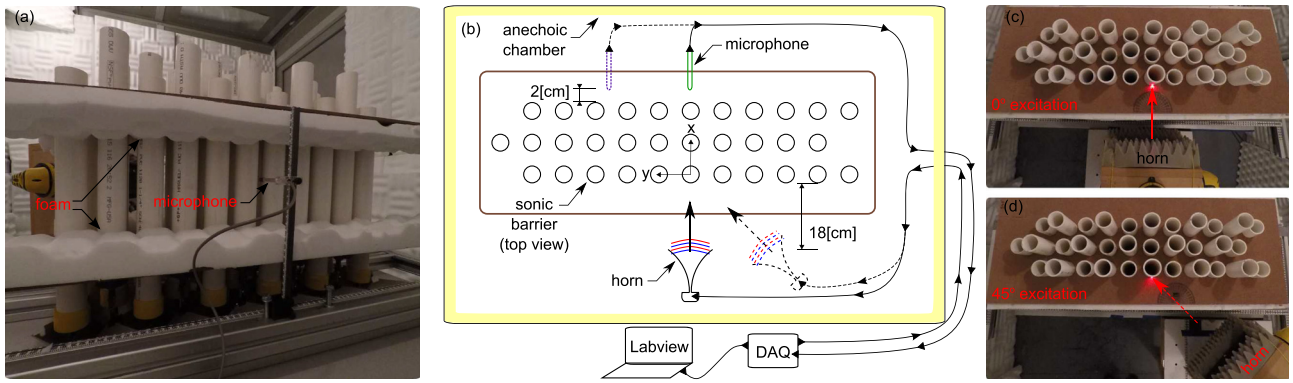

FIG. 7. Origami sonic barrier (OSB) at 55° folding configuration. (a) Side view displays the foam used for absorbing any oblique incident waves, and also shown is the location of the microphone for 0° wave excitation. (b) This schematic of top view shows the geometric locations and orientation of a horn-mic setup for 0° and 45° wave excitations. (c) and (d) show the orientation of the horn and the sound propagation direction with respect to the barrier, during the test for different wave incidence tests.

(red) line is the threshold limit set for insertion loss [12 (dB)]. Furthermore, the horizontal dash-dotted (black) lines are provided that act as a guide to identify the spectral regions, where the IL of barrier is greater than the threshold for both directions of excitation.

In Figs. 8(b) and 8(d), dispersion diagrams (generated via PWE) of the scaled-down sonic barrier are plotted, where the region between the horizontal dash-dotted (blue) lines represents the region of complete bandgap. The materials properties used for evaluating the band structure via the PWE method (Appendix A) in the 2D cross-section plane are given in Table I, and the outer radius of PVC inclusions are assigned to be 0.0211 (m). Because of the large impedance mismatch between PVC inclusions and the air host, most of the wave energy incident on the inclusion-host interface is reflected back into the air, and hence with little energy transfer into the inclusions, we modelled hollow PVC pipes as a solid PVC rod. Furthermore, the air is assumed to be ideal with non-dispersive characteristics while evaluating the band structure. As will be shown later, the PWE results match well with the experimental data, validating the accuracy of the above assumptions.

Upon comparing the experimental IL spectra [Fig. 8(a) and 8(c)] to the dispersion diagrams [Figs. 8(b) and 8(d)], it can be clearly observed that the complete bandgap predicted via the PWE method aligns very well with the peaks of the IL between the horizontal black dash-dotted lines. Furthermore, comparing the IL of an OSB at different folding configurations [Figs. 8(a) and 8(c)], it can be observed that the sound blocking performance occurs in different spectral regions—i.e., the scaled-down OSB at 55° folding angle can block low frequency waves [around 3.5 (kHz)], while the same barrier at 70° folding angle can block the high frequency wave propagation i.e., around 7 (kHz).

Based on the experiments of a scaled-down model and the simulation results as presented in Sec. III of this article, it can be concluded with confidence that the sound blocking features of an actual size origami sonic barrier can be tuned in the frequency range 500–1200 (Hz). The above statements imply that the origami sonic barrier configured to 55° folding angle with a square lattice can be used to block low frequency dominated traffic noise (that occurs on highways during rush-hour or on roads with heavy-vehicle traffic), while on the other hand, the reconfigured sonic barrier to 70°

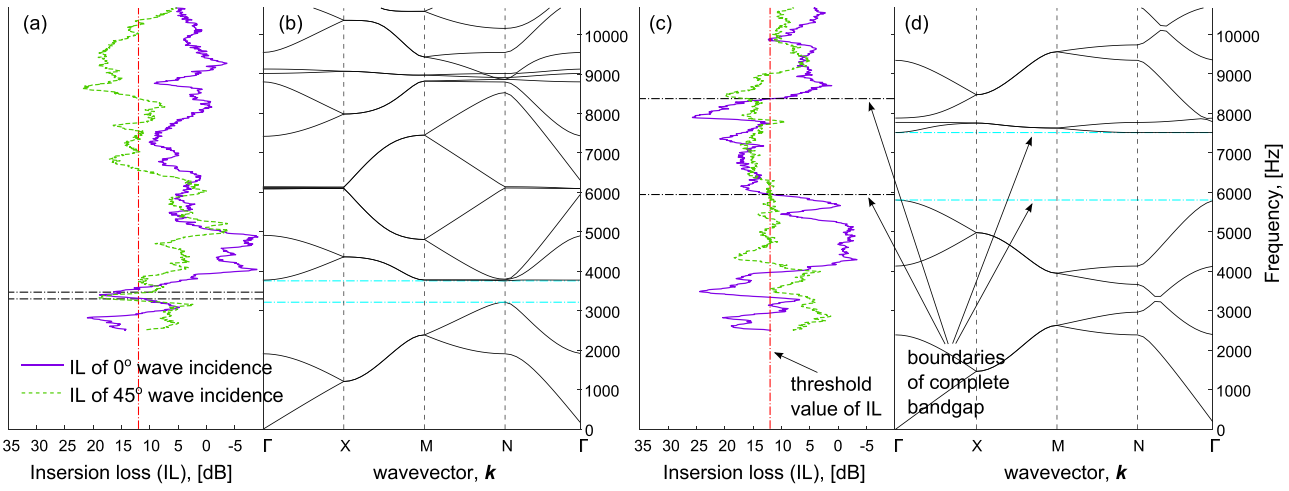

FIG. 8. (a) and (c) are the experimentally calculated insertion loss (IL) spectra, and (b) and (d) are the dispersion diagrams generated via the PWE method of a scaled-down origami sonic barrier (OSB) at 55° and 70° folding angles respectively. In (a) and (c), two different IL curves correspond to 0° and 45° wave incidence.

folding angle with a hexagonal lattice can block high frequency dominated traffic noise (that occur on highways during off-peak traffic and on roads with automobile traffic).

One other important feature of the origami sonic barrier is that the reconfiguration mechanism that causes the wave adaptability is a one-degree of freedom action and thus requires low actuation effort to precisely reconfigure the barrier. Furthermore, with an inherent rugged top edge profile, the OSB can better-diffuse the diffracted wave at the top edge (compared to a vertical wall barrier of same height), leading to reduced transmission of an oblique incident wave across the barrier. Additionally, the OSB with its corrugated façade, perpendicular to wave propagation, leads to better diffusivity of the wave that is reflected into the road;[12] such phenomena of radiating the sound energy in many directions is an important property that is required for reflective sound barriers for reducing the intensity of reflected sound on the road side. Hence, the origami sonic barrier with the advantages of a periodic barrier, coupled with better diffusion properties and *tunable* wave blocking characteristics at limited actuation, will be an effective innovation for attenuating complex traffic noise.

V. CONCLUSIONS

A concept of origami sonic barrier is proposed, which exploits origami folding for lattice reconfiguration and achieves adaptable sound blocking characteristics. Analytical and numerical investigation results generated using the PWE method and COMSOL software show that the dispersion characteristics and the insertion loss of the origami sonic barriers can be tuned in the desired frequency range of traffic noise spectra. Further, experiments performed on a scaled-down model demonstrate that the origami sonic barrier can be reconfigured between different Bravais lattices, and that a full-scale origami sonic barrier can be tuned to attenuate the complex noise pollution spectra, whose dominant frequency shifts in the range of 500 to 1200 (Hz). The tunable wave characteristics together with the benefits of a periodic barrier and a practical actuation mechanism make the origami sonic barrier a prime candidate for attenuating traffic noise.

ACKNOWLEDGMENTS

The authors would like to thank Dr. Karl Grosh and his lab at the University of Michigan for allowing us to use their anechoic chamber and providing us with the microphones and horns. We would also like to thank Dr. Suyi Li from Clemson University for his valuable input on the design of test setup. This research was partially supported by the University of Michigan Collegiate Professorship and the National Science Foundation under Award No. 1634545.

APPENDIX A: PLANE WAVE EXPANSION METHOD

The fundamental idea behind the PWE method is to expand the periodically varying materials properties ($\rho_{\text{inv}} = \frac{1}{\rho}$, $K_{\text{inv}} = \frac{1}{\rho c_l^2}$) in Eq. (3) as Fourier series, in terms of unit cell parameters and with plane waves being used as basis functions, as given in Eq. (A1); where τ is the place holder for K_{inv} and ρ_{inv}, and τ_G being their Fourier coefficient. The wave numbers of the plane waves in the expansion are given by reciprocal lattice vectors, $\vec{b_1}$ and $\vec{b_2}$, with (m, n) being integers, spanning from $-q$ to q.

$$\begin{aligned}
\tau(\vec{x}) &= \sum_G \tau_G e^{i\overline{G}.\overline{x}}, \\
\tau_G &= \frac{1}{A_{cell}} \int\int_{A_{cell}} \tau(\overline{x}) e^{-i\overline{G}.\overline{x}} dA, \\
\overline{G} &= m\overline{b_1} + n\overline{b_2}, \\
\overline{b_1} &= \frac{2\pi}{|\overline{a_1}|}\hat{x} \;\&\; \overline{b_2} = \frac{2\pi}{|\overline{a_2}|}\hat{y}.
\end{aligned} \tag{A1}$$

Now, the pressure field in Eq. (3) can also be expanded using Floquet-Bloch theorem, which states that the wave field in a periodic structure is entirely periodic except for the phase shift across the unit cell, as $p(\overline{x}) = \sum_G p_G e^{i\overline{G}.\overline{x}} e^{i\overline{k}.\overline{x}}$, where $\overline{k}$ is the wavevector. The wavevector is typically swept along the edges of the irreducible 1st Brillouin zone to evaluate the bandgap structure; for the unit cell considered, the high symmetry wavevector directions are represented by sides of the rectangle, ΓXMNΓ with $\Gamma = (0, 0)$, $X = \left(\frac{\pi}{|\overline{a_1}|}, 0\right)$, $M = \left(\frac{\pi}{|\overline{a_1}|}, \frac{\pi}{|\overline{a_2}|}\right)$, $N = \left(0, \frac{\pi}{|\overline{a_2}|}\right)$, as shown in the inset of Fig. 4(a).

Furthermore, the Fourier coefficient τ_G in Eq. (A1), for circular inclusion, can be simplified as

$$\begin{aligned}
\overline{\tau}_{\overline{G}=0} &= \frac{1}{A_{cell}} \left(\sum_{inc=1}^{total\#\,of\,inc} \left(A_{inc}(\tau_{inc} - \tau_{host})\right) + A_{cell}\tau_{host} \right), \\
\overline{\tau}_{\overline{G}\neq 0} &= \frac{1}{A_{cell}} \left(\sum_{inc=1}^{total\#\,of\,inc} \left(J(|\overline{G}|R_{inc}) e^{-i|\overline{G}|.\overline{C}_{inc}} \frac{2\pi}{|\overline{G}|} R_{inc}(\tau_{inc} - \tau_{host}) \right) \right),
\end{aligned} \tag{A2}$$

where J is the Bessel function of the 1st kind of order 1, "*inc*" represents the equivalent inclusions and R is the radius of the circular inclusion.

Upon substitution of materials properties and pressure field expansions into Eq. (3), Eq. (3) is discretized into the eigen value problem (EVP) $\left[P^{-1}Q - \omega^2 I\right] p_G = 0$, with P and Q representing $(2q+1)^2$ square matrices, $p_{ij} = K_{inv\overline{G_i}-\overline{G_j}}$; $Q_{ij} = \left(\overline{k} + \overline{G_j}\right).\left(\overline{k} + \overline{G_i}\right)\rho_{inv\overline{G_i}-\overline{G_j}}$. For the kind of periodic distribution of circular inclusions given in Fig. 4(a), a value of q equal to 9 [i.e., 361 number of plane waves for Fourier expansions of Eq. (A1)] provided reliably good convergence of eigen values at minimum computational cost.[27] The EVP is solved along different wavevectors spanning the edges of the irreducible 1st Brillouin zone, and a typical dispersion diagram which represents the first few eigen frequencies along the high symmetry directions is extracted.

[1]T. K. Swinburn, M. S. Hammer, and R. L. Neitzel, "Valuing quiet: An economic assessment of U.S. environmental noise as a cardiovascular health hazard," Am. J. Prev. Med. **49**(3), 345–353 (2015).
[2]L. Goines and L. Hagler, "Noise pollution: A modern plague," South. Med. J. **100**(3), 287 (2007).
[3]G. Sheng, *Vehicle Noise, Vibration, and Sound Quality* (SAE International, Warrendale, 2012).

[4]J. L. Rochat and D. Reiter, "Highway traffic noise," Acoust. Today **12**(4), 38 (2016).
[5]A. Can, L. Leclercq, J. Lelong, and D. Botteldooren, "Traffic noise spectrum analysis: Dynamic modeling vs. experimental observations," Appl. Acoust. **71**(8), 764 (2010).
[6]T. Ogle, R. Wayson, and W. Lindeman, "Effect of vehicle speed on sound," J. Transp. Res. Board **1559**, 14 (1996).
[7]P. Menounou and J. Ho You, "Experimental study of the diffracted sound field around jagged edge noise barriers," J. Acoust. Soc. Am. **116**(5), 2843–2854 (2004).
[8]J. Parnell, S. Samuels, and C. Tsitsos, "The acoustic performance of novel noise barrier profiles measured at the roadside," Acoust. Aust. **38**(3), 123–128 (2010).
[9]S. S. T. Ho, I. J. Busch-Vishniac, and D. T. Blackstock, "Noise reduction by a barrier having a random edge profile," J. Acoust. Soc. Am. **101**(5), 2669–2676 (1997).
[10]F. Morandi, A. Marzani, S. De Cesaris, D. D'Orazio, L. Barbaresi, and M. Garai, "Sonic crystals as tunable noise barriers," Riv. Ital. Acust. **40**(4), 1–19 (2016).
[11]M. P. Peiró-Torres, J. Redondo, J. M. Bravo, and J. V. Sánchez-Pérez, "Open noise barriers based on sonic crystals. Advances in noise control in transport infrastructures," Transp. Res. Procedia **18**, 392 (2016).
[12]P. Amado-Mendes, L. Godinho, P. G. Santos, A. G. Dias, and M. Martins, "Laboratory and full-scale experimental evaluation of the acoustic behaviour of sonic crystal noise barriers crystal noise barriers," in Proceedings of the International Congress on Acoustics (2016).
[13]L. Godinho, P. G. Santos, P. Amado-Mendes, A. Pereira, and M. Martins, "Experimental and numerical analysis of sustainable sonic crystal barriers based on timber logs," in EuroRegio (2016).
[14]C. Rubio, A. Uris, P. Candelas, F. Belmar, and V. Gomez-Lozano, "A tunable acoustic barrier based on periodic arrays of subwavelength slits," AIP Adv. **5**(5), 57150 (2015).
[15]S. Castiñeira-Ibañez, C. Rubio, and J. V. Sánchez-Pérez, "Environmental noise control during its transmission phase to protect buildings. Design model for acoustic barriers based on arrays of isolated scatterers," Build. Environ. **93**, 179 (2015).
[16]M. Martins, J. Carbajo, L. Godinho, P. Amado-Mendes, and J. Ramis, "Insertion loss provided by a periodic structure - numerical and experimental evaluation," in Tecni Acustica (2013).
[17]V. Romero-García, A. Krynkin, L. M. García-Raffi, O. Umnova, and J. V. Sanchez-Perez, "Multi-resonant scatterers in sonic crystals: Locally multi-resonant acoustic metamaterial," J. Sound Vib. **332**, 184 (2013).
[18]F. Koussa, J. Defrance, P. Jean, and P. Blanc-Benon, "Transport noise reduction by low height sonic crystal noise barriers," in Proceedings of the Acoustics (2012).
[19]V. Romero-García, J. V. Sánchez-Pérez, and L. M. García-raffi, "Tunable wideband bandstop acoustic filter based on two-dimensional multiphysical phenomena periodic systems," J. Appl. Phys. **110**, 14904 (2011).
[20]A. Y. B. Chong, K. Attenborough, and S. Taherzadeh, "The performance of vertical and horizontal sonic crystal noise barriers above a ground surface," in Internoise (2010).
[21]T. Miyashita, "Sonic crystals and sonic wave-guides," Meas. Sci. Technol. **16**, R47 (2005).
[22]J. V. Sánchez-Pérez, C. Rubio, R. Mártinez-Sala, R. Sánchez-Grandia, and V. Gomez, "Acoustic barriers based on periodic arrays of scatterers," Appl. Phys. Lett. **81**(27), 5240–5242 (2002).
[23]J. V. Sánchez-Pérez, C. R. Michavila, L. M. García-Raffi, V. Romero-García, and S. Castiñeira-Ibáñez, "Noise certification of a sonic crystal acoustic screen designed using a triangular lattice according to the standards EN 1793 (-1;-2;-3)," in EuroNoise (2015).
[24]F. Morandi, S. De Cesaris, M. Garai, M. Miniaci, and A. Marzani, "Experimental evidence of band gaps in periodic structures," in Euronoise (2015).
[25]M. Thota, S. Li, and K. W. Wang, "Lattice reconfiguration and phononic bandgap adaptation via origami folding," Phys. Rev. B **95**(6), 64307 (2017).
[26]M. M. Sigalas and E. N. Economou, "Attenuation of multiple-scattered sound," Europhys. Lett. **36**(4), 241–246 (1996).
[27]M. S. Kushwaha, "Stop-bands for periodic metallic rods: Sculptures that can filter the noise," Appl. Phys. Lett. **70**(24), 3218–3220 (1997).
[28]L. Brillouin, *Wave Propagation in Periodic Structures*; electric filters and crystal lattices, 1st ed. (McGraw-Hill Book Company, Inc., New York, NY, 1946).
[29]See https://vancampenbayards.com/en/projects/363-a2-noise-barrier-pipes-screen-eindhoven for a video of periodic sound barrier.